

ARTICLE

Two-dimensional Porous Silicon Nanosheets as Anode Materials for High Performance Lithium-ion Batteries

Jingjing Tang,^{a,d,1} Qifang Yin,^{a,1} Qian Wang,^a Qianqian Li,^b Hongtao Wang,^c Zhenglong Xu,^a Haimin Yao,^{*a} Juan Yang,^d Xiangyang Zhou,^d Jang-Kyo Kim^e and Limin Zhou^{*a}

Received 00th January 20xx,
Accepted 00th January 20xx

DOI: 10.1039/x0xx00000x

Silicon nanosheets (Si-NSs) are chemically synthesized using graphene oxide nanosheets as the template. The obtained Si-NSs, which are aggregations of silicon nanocrystals with size of ~10 nm, are applied directly as anode material for lithium ion batteries, delivering a reversible capacity of 800 mAh g⁻¹ after 900 cycles at a rate as high as 8400 mA g⁻¹. Ex-situ measurements and in-situ observations certify the positive effect of mesoporous structure on the structural stability of Si-NSs. The evolution and survivability of the porous structures during lithiation and delithiation cycling are investigated by molecular dynamics simulations, demonstrating that the porous structure can enhance the amount of “active” Li atoms during the stable stage of cycling and promote mass capacity, and the prolonged survival of porous structure helps retain high mass capacity.

Introduction

Lithium ion batteries (LIBs) are deemed as one of the most practical and effective technologies for electrochemical energy storage.¹ They are widely used in a variety of household electronics, portable electric devices, electric vehicles and so on. Therefore, developing LIBs with high energy density and excellent cycling stability becomes critical and urgent for meeting the continuously increasing energy demands.² The negative electrode material in current commercial LIBs is mainly graphite, which has a limited theoretical capacity of 372 mAh g⁻¹.³ Enormous efforts have been made to develop new negative electrode materials with high specific capacity and high cycling stability, such as silicon-based and tin-based nanomaterials,⁴⁻⁶ metal oxides and related composites,⁷⁻¹⁰ and nano carbon materials.^{11,12} Particular attention has been paid to Si for its high theoretical capacity (4200 mAh g⁻¹ for Li_{4.4}Si), low reaction potential (~0.5 V versus Li/Li⁺) and abundance of reserve in the earth. Therefore, Si has been regarded as one of the most promising anode candidates for the next-generation LIBs. However, the huge volume expansion (>300 %) during the lithiation process causes severe structural damage, extremely

unstable solid electrolyte interphase (SEI) and significant capacity fade, which hinder the practical applications of Si in LIBs.^{13,14} Many approaches have been proposed to tackle these tough issues of Si. Reducing the Si dimensions to nano- or subnano-scale is one of them. Moreover, studies on constructing Si nanowires, nanotubes, hollow and porous spheres, and core-shell and yolk-shell nanostructures have also shown discernible progress.¹⁵⁻²⁰ For instance, Si nanowires delivered a reversible capacity of ~1000 mAh g⁻¹ with 90 % capacity retention over 100 cycles.²¹ Hollow Si spheres with inner radius of 175 nm and outer radius of 200 nm exhibited a reversible capacity of 2725 mAh g⁻¹ and 48 % capacity degradation after 700 cycles.¹⁷ However, the fabrications of Si nanostructures often apply chemical vapor deposition (CVD) which involves the use of toxic and expensive precursors. Therefore, environmentally friendly, cost-effective and scalable synthesis of Si nanostructures with outstanding electrochemical performance is still a challenge. As a typical low-dimensional nanostructure, two-dimensional (2D) materials, owing to their nanoscale thickness and microscopic lateral dimensions, have shown many unprecedented properties and been explored for potential applications in lithium-ion storage.²²⁻²⁴ For example, Park et al. prepared Si-NSs via chemical reduction of natural clays and used them as anode materials of LIBs. The initial Coulombic efficiency obtained was only 42.4 % and the cycling stability degraded rapidly.²⁵ Hong et al. improved the cycling performance of sand-induced Si-NSs by encapsulating the reduced graphene oxide and achieved a reversible capacity of ~1500 mAh g⁻¹ after 50 cycles.²⁶ However, the initial Coulombic efficiency was unsatisfactory and the long-term cycling performance was still poor.

In recent years, porous Si nanostructures have attracted increasing attention because of their superior capability to accommodate the volume expansions of Si and therefore

^a Department of Mechanical and Engineering, The Hong Kong Polytechnic University, Hong Kong, China

^b Materials Genome Institute, Shanghai University, Shanghai, China

^c Institute of Applied Mechanics, Zhejiang University, Hangzhou, China

^d School of Metallurgy and Environment, Central South University, Changsha, China

^e Department of Mechanical and Aerospace Engineering, Hong Kong University of Science and Technology, Clear Water Bay, Hong Kong, China

Electronic Supplementary Information (ESI) available: The nitrogen adsorption isotherm and respective calculated PSD of m-SiO₂, cycling performance of the tested Si-NSs anode after it is let stand for 10 days, images of Si-NSs and commercial nano Si electrodes after 100 cycles, and the comparison of electrochemical performance of reported bare nano-Si and Si-based nanocomposites can be found in the Supporting Information Available online. The in-situ TEM video of m-Si (video) is also available free of charge. See DOI: 10.1039/x0xx00000x

enhance the cycling stability. Moreover, porous structure can create efficient channels for the rapid transport of lithium ions and facilitate the transport of electrons and ions throughout the electrode. Yang et al. synthesized a mesoporous Si anode using SBA-15 silica as Si source, showing a high initial capacity of 2727 mAh g⁻¹. However, the capacity dropped quickly and the capacity retention at the 100th cycle was only 53 % against that of the 2nd cycle.²⁷ Zhou et al. reported a mesoporous Si nanowires anode material via metal-assisted chemical etching process, which exhibited a reversible capacity of 1000 mAh g⁻¹ at 1 C and good cycling stability.²⁸ Nevertheless, the costly synthesis process cannot meet the requirements from industries. More recently, Yang et al. prepared a porous Si material by a solvothermal reaction followed by a high-temperature annealing process, showing a reversible capacity of 1577 mAh g⁻¹ at 1 A g⁻¹ and outstanding rate performance.²⁹ However, the complicated preparation procedure, toxic and expensive Si source may hinder its mass production.

Herein, silicon nanosheets (Si-NSs) anode with porous structure was fabricated and evaluated as anode material for LIBs. Ex- and in-situ characterizations were carried out to study the structural features of the material. Besides, the evolution and survivability of the porous structures during the lithiation and delithiation cycling were investigated using molecular dynamics simulations. The result of this study can serve as guideline for the design and fabrication of the Si-based anode material for the next-generation LIBs.

Experimental sections

The Preparation of GO

Graphite oxide is first synthesized from natural graphite flakes based on a modified Hummers method.^{30,31} The prepared graphite oxide is dispersed in deionized water by ultrasonication to get the homogeneous GO aqueous dispersion for use.

The Synthesis of GO/SiO₂

Silica layers are grown on the surfaces of GO nanosheets via the hydrolysis of TEOS. Typically, NaOH (0.1 g) and cetyltrimethylammonium bromide (CTAB) (2 g) are dissolved in GO dispersion (400 mL) under mechanical stirring to form a brown solution. Subsequently, TEOS (5 mL) is dropped into the brown solution (GO/NaOH/CTAB) under stirring, and the reaction mixture was stirred for 10 h at a temperature of 40 °C. GO/SiO₂ is collected by centrifugation, washed thoroughly with diluted HCl, ethanol and deionized water, and finally freeze dried.

The Synthesis of m-SiO₂ and Si-NSs

m-SiO₂ is prepared through a one-step calcination of GO/SiO₂ in a furnace under a flow of dry air at 750 °C and stabilized for 2 h. Si-NSs are synthesized by the magnesiothermic reduction method. In a typical preparation, m-SiO₂ powder, NaCl and Mg in weight ratio 1:10:0.9 are mixed and loaded into a Swagelok-type reactor under the protection of Ar atmosphere. The sealed reactor is loaded in a tube furnace and heated at 700 °C for 6 h under an Ar atmosphere. After cooling down to room temperature, Si-NSs are obtained after washed with diluted HCl

and HF solution to remove MgO and residual SiO₂, respectively. For comparison, the sample produced without adding NaCl while keeping all other preparation conditions unchanged, is prepared and designated as Si-W/O-NaCl.

Characterization

Field emission scanning electron microscopy (SEM) measurements are conducted on a Helios FIB 600i field emission scanning electron microscope operated at 15 kV. Field emission transmission electron microscopy (TEM) and high resolution TEM (HRTEM) characterizations are performed on a Titan G2 60-300 field emission transmission electron microscope operated at 200 kV. Nitrogen adsorption and desorption isotherms are obtained using a Micromeritics ASAP 2020 system. The pore size distribution (PSD) is calculated from the adsorption branch using the Barrett-Joyner-Halenda method. X-ray powder diffraction (XRD) measurements are performed on a Rigaku-TTRIII diffractometer using Cu K α radiation.

Electrochemical measurement

Electrochemical experiments are performed using CR2025 coin-type cells. To prepare working electrodes, Si-NSs, acetylene carbon black and sodium alginate binder in mass ratio 3:1:1 are mixed with deionized water sufficiently with pestle and mortar. The obtained slurry is pasted onto a Cu foil and dried overnight at 80 °C in a vacuum oven. The dried electrode is assembled into a half-cell in an ultra-pure argon filled glove box with a lithium foil used as the counter electrode and 1 M LiPF₆ in ethylene carbonate and diethyl carbonate (EC:DEC = 1:1) with a 10 vol.% fluoroethylene carbonate (FEC) additive as the electrolyte. The typical loading of the active Si-NSs on the electrode was 0.8 mg cm⁻². Cells are assembled in an ultra-pure argon filled glove box. Galvanostatic discharging-charging is carried out on a LAND CT-2001A in the potential range 0.01-1.2 V (vs. Li⁺/Li). Cyclic voltammograms (CV) experiment is performed on an electrochemical workstation (P4000) with a potential window range 0.01-1.2 V (vs. Li⁺/Li) at a scan rate of 0.1 mV s⁻¹. The rate capability is calculated based on the theoretical capacity of Si (1 C = 4200 mA g⁻¹).

MD simulations

Molecular Dynamics simulation is conducted by using the Large-scale Atomic/Molecular Massively Parallel Simulator (LAMMPS) package³² with charge equilibrium toolkit³³⁻³⁵ is used to conduct to Molecular Dynamics simulation. The interaction between Si and Li is described by the reactive force field (ReaxFF) potential,³⁶ which has been proved applicable in simulating the alloying process of Li and Si.³⁶⁻⁴³ The porous structure inside the Si-NSs is modelled by introducing a series of periodically distributed pores of the same size (see Fig. 6a). The unit cell with one single pore is created by removing atoms from a single crystalline Si cube with dimension of ~7 nm in each direction (Fig. 6b and c). Periodic boundary

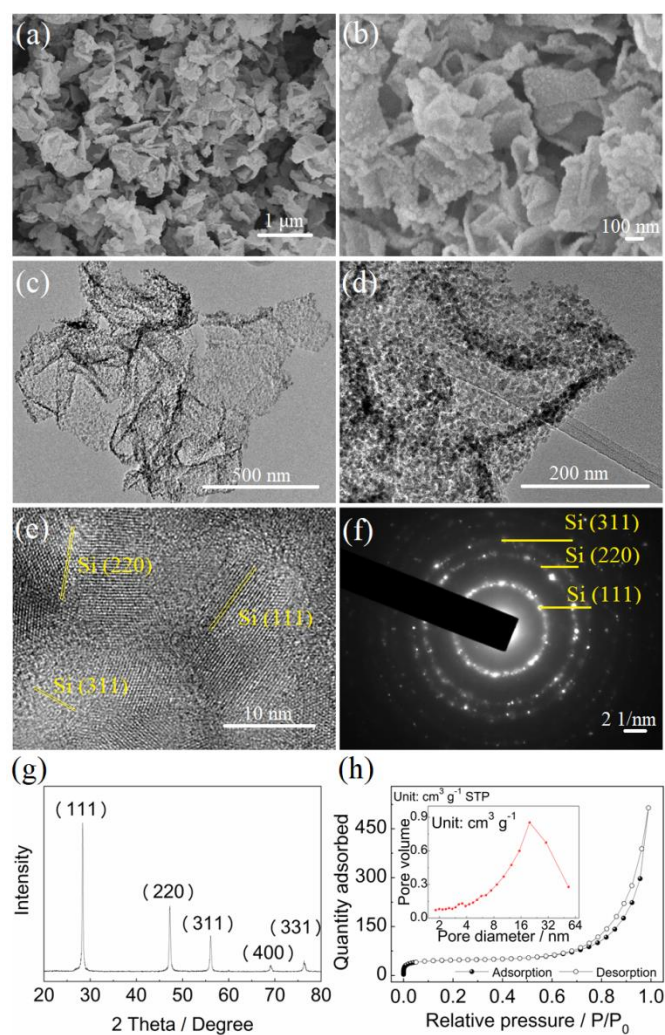


Fig. 1. Characterization of Si-NSs. (a, b) SEM images, (c, d) TEM images, (e) HRTEM image, (f) SAED pattern, (g) XRD pattern, (h) N_2 sorption isotherm and the corresponding pore-size distribution (inset).

conditions are applied in both in-plane directions. The out-of-plane direction is along [010] orientation of Si crystal. As indicated by the SEM image in Fig. 1a, lithiation and delithiation should occur on both sides of the sheet; so in order to save the computation time, the calculation model is further simplified by using a reflective boundary condition based on the physical and geometrical symmetry in [010] direction of the sheet. The simulations of lithiation-delithiation cycles are carried out at a temperature of 300 K with Berendsen thermostat⁴⁴ and the time step is 0.2 fs.⁴⁰ The possible interaction of the anode with the surrounding substances such as binder or carbon black is neglected^{36,38-42} and thus the sheet can deform along all directions without any mechanical constraints. This treatment is consistent with the morphology of the porous Si-NSs anode shown in the SEM image (Fig. 3a). In simulations, lithiation can spontaneously happen when the Li atoms touch the Si cell,^{36,39-42} while delithiation is achieved by randomly removing Li atoms from the lithiated Si.⁴² Software of OVITO is used for visualization and post-processing.⁴⁵

Results and Discussions

Two-dimensional graphene oxide supported silica (GO/SiO₂) is firstly fabricated via the hydrolysis of tetraethylorthosilicate (TEOS) with the aid of cetyltrimethyl ammonium bromide (CTAB) as the surfactant. Mesoporous silica (m-SiO₂) is obtained by the calcination of GO/SiO₂ under air atmospheres. Then, Si-NSs are synthesized via the magnesiothermic reduction of m-SiO₂ with the assistant of NaCl as the heat scavenger. More details are available in Experimental Section and Supplementary Material.

Characterization of the Porous Si-NSs

The morphology of the obtained GO, GO/SiO₂ and m-SiO₂ is examined by scanning electron microscope (SEM) and transmission electron microscope (TEM). The as-prepared GO manifests a typical 2D wrinkled and thin sheet-like structure with the lateral size up to 10 μm as shown in Fig. S1a and b. The inset of Fig. S1b shows the selected-area electron diffraction (SAED) pattern of GO, and the sharp diffraction pattern implies the crystalline structure of carbon in GO.⁴⁶ Fig. S1c and d show the SEM and TEM images of GO/SiO₂. It is apparent that GO/SiO₂ is composed of many free-standing 2D sheet-like plates with lateral size up to 1 μm, demonstrating that GO matrix are ripped into small pieces during the attaching of SiO₂. Compared with the bare GO, there is an obvious increase in the cross section. Besides, no free silica particles or naked GO sheets are detected, demonstrating the perfect coating of silica layer on GO. The resulting m-SiO₂ sheets after the removal of GO possess a wrinkled structure and the obtained silica nanosheets is about 50 nm in thickness as shown in Fig. S1e and f and Fig. S3a. The elemental composition of the as-prepared m-SiO₂ are analysed with the aid of XPS. As illustrated in the survey XPS spectra in Fig. S2a, Si 2p, Si 2s, O 1s and O KLL with narrow sharp peaks were observed in m-SiO₂. Besides, trace amount of C is also detected as shown by the C1s peak at ~284.6 eV, which should be ascribed to the highly sensitive detection capability of XPS (The application of carbon conductive adhesive may be scanned by XPS). The Si 2p and O 1s peaks centred at 103.4 eV and 533.1 eV further confirm the pure silica phase in m-SiO₂. Nitrogen adsorption-desorption measurements are carried out for m-SiO₂ as present in Fig. S2b, which displays a representative type IV isotherm characterized by the H2 hysteresis loop, indicating the mesoporous structure of m-SiO₂. The BET surface area and total pore volume for m-SiO₂ are calculated to be 797 m² g⁻¹ and 0.89 cm³ g⁻¹, respectively. From Fig. S2c, it can be seen the Barrett-Joyner-Halenda (BJH) pore size of m-SiO₂ is in the range of 2-4 nm, which is consistent with the HRTEM image (Fig. S1h). Si-NSs are synthesized via magnesiothermic reduction of m-SiO₂ with NaCl used as the heat scavenger. The morphology and the crystalline structure of the obtained Si-NSs are shown in Fig. 1. After the reduction, Si-NSs maintain the original 2D sheet-like structure with rough surface, which is ascribed to

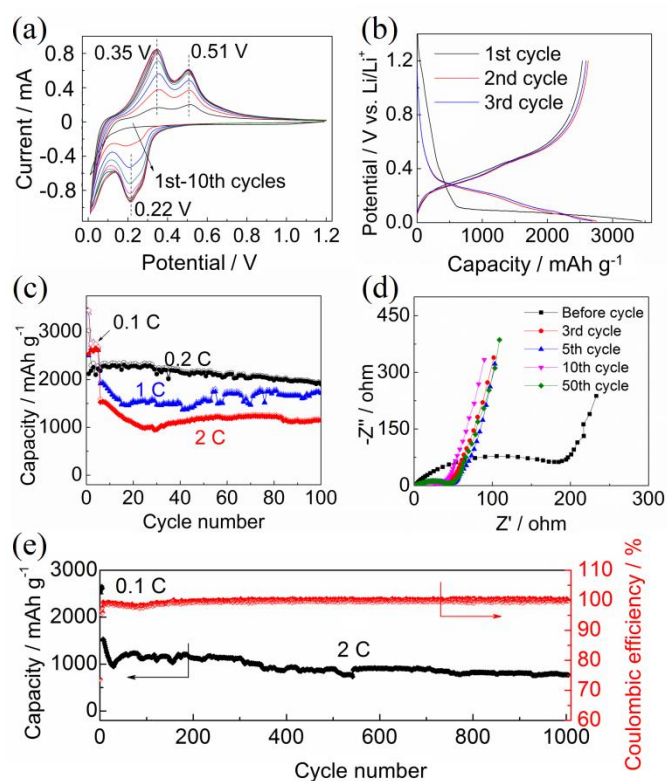


Fig. 2. (a) Cyclic voltammety characteristics of Si-NSs; (b) Charge-discharge curves of Si-NSs electrodes at a current density of 0.1 C; (c) Cycling performance of Si-NSs at different rates, and the cells are cycled at 0.1 C for the first 5 cycles and 1 C or 2 C for the later cycles; (d) Nyquist plots of Si-NSs electrode for selected cycles; (e) Delithiation cycling performance and Coulombic efficiency of Si-NSs at high current density of 2 C, and the initial 5 cycles are tested at a rate of 0.1 C (1 C = 4200 mA g⁻¹).

the aggregation of Si nanocrystals (see Fig. 1a and b). The thickness of the obtained Si-NSs is about 30 nm as shown in Fig. S3b. To demonstrate the heat-scavenging effect by the NaCl additive on the morphology of Si products, m-SiO₂ nanosheets are also thermally reduced by Mg without addition of NaCl and the obtained Si is characterized by SEM (see Fig. S4). It is evident that the original sheet-like structure is destroyed and the obtained Si product denoted as Si-W/O-NaCl exhibits a disordered morphology. This is attributed to the collapse of m-SiO₂ and the agglomeration of the as-synthesized Si domains due to the massive heat release from the reaction of magnesiothermic reduction.⁴⁷ The TEM images shown in Fig. 1c and d further demonstrate the highly porous structure of the Si-NSs sample. High resolution TEM (HRTEM) observation (see Fig. 1e) indicates that Si-NSs are composed of interconnected silicon nanocrystals with size of ~10 nm and lattice fringe spacing of ~0.32 nm which is consistent with spacing between (111) planes of polycrystalline silicon. Fig. 1f shows the SAED pattern of Si-NSs, indicating the typical (111), (220) and (311) diffraction rings of polycrystalline silicon. X-ray powder diffraction (XRD) measurement is performed to further characterize the phase and purity of Si-NSs. As shown in Fig. 1g, the (111), (220), (311),

(400) and (331) peaks imply the high crystallinity of silicon. Given the location of $2\theta = 28^\circ$ for the (111) peak and the wavelength of the applied radiation $\lambda = 0.154$ nm (Cu K α), application of the Bragg's law gives a lattice fringe spacing of ~0.32 nm, which is in good agreement with the measurement from the HRTEM image (Fig. 1e). The pore structure of Si-NSs is further investigated by nitrogen adsorption-desorption isotherm measurement. The results are shown in Fig. 1h. The BET surface area of Si-NSs is 146 m² g⁻¹ and the main pore size distribution is in the range of 16-32 nm (Fig. 1h inset). Based on the BJH theory, the average pore size and the pore volume per unit mass can be estimated as about 20 nm and 0.8 cm³ g⁻¹, respectively. To examine the electrochemical performance of the as-prepared 2D porous Si-NSs, coin-type half-cells are constructed by using them as the anode active materials and Li metal as the counter electrode (see Methods for details). Fig. 2a shows the initial 10 cycles of the cyclic voltammety characteristics obtained at a scan rate of 0.1 mV s⁻¹ with a potential range of 0.01-1.2 V. One pronounced cathodic peak at 0.22 V and two anodic peaks at 0.35 V and 0.51 V can be ascribed to the lithiation and delithiation process, respectively.⁴⁸ The increase of the CV peak intensity indicates the occurrence of activation process over the first few cycles. Fig. 2b displays the typical voltage capacity profiles of the Si-NSs anode at the discharge-charge rate of 0.1 C. The Si-NSs electrode exhibits an initial discharge capacity (lithiation capacity) of 3448 mAh g⁻¹, which is nearly 82% of its theoretical value (4200 mAh g⁻¹). The irreversible capacity loss in the first cycle (26%) is mainly attributed to the formation of the SEI layers, which agrees well with the results of the CV studies. The discharge capacity of the 2nd and 3rd cycles remains stable at 2754 and 2692 mAh g⁻¹, with the corresponding charge capacity (delithiation capacity) being 2627 and 2594 mAh g⁻¹, respectively. Thus, much higher coulombic efficiency of 95% and 96% can be obtained, indicating the superior Li-ions insertion-extraction reversibility in the Si-NSs electrode. The cycling performance of the Si-NSs electrodes at different current densities of 0.2 C, 1 C and 2 C in the voltage range of 0.01-1.2 V is shown in Fig. 2c. At the current density of 0.2 C, the Si-NSs electrode delivers an initial charge capacity of 2118 mAh g⁻¹ with a coulombic efficiency of 70%. The reversible capacity of Si-NSs anode increases in the initial several cycles and retains almost 100% capacity until 29 cycles. Moreover, after 100 deep discharge-charges cycles, a reversible charge capacity of 1901 mAh g⁻¹ is obtained with a fading rate as low as 0.1% per cycle. Although the charge capacities decrease when the rates increase to 1 C and 2 C, high capacity retentions are detected. After being activated for the initial 5 cycles at a rate of 0.1 C for the formation of a stable SEI layer, the reversible capacities of Si-NSs electrodes at the 6th cycles are 1913 and 1525 mAh g⁻¹, respectively. After 100 cycles, the reversible capacities of Si-NSs are 1712 and 1150 mAh g⁻¹ at the rate of 1 C and 2 C, respectively. It is worthy to note that these levels of capacity retention are achieved without applying additional carbon coating. The electrochemical impedance spectra (EIS) measurement of Si-NSs electrode is conducted to analyze the discharge-charge

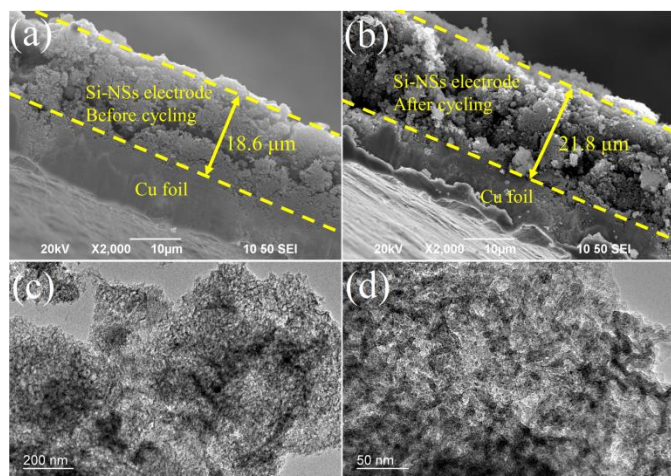


Fig. 3. Cross-sectional SEM images of Si-NSs (a) before and (b) after 100 cycles at 0.2 C; (c, d) TEM images of Si-NSs after cycling.

kinetics. The Nyquist plots of Si-NSs electrode before cycling and after 3, 5, 10 and 50 cycles are shown in Fig. 2d. The decreased semicircle at the high frequency after cycling demonstrates the small charge transfer resistance, which implies a good cycling performance of Si-NSs electrode. Fig. 2e shows the cycling performance and coulombic efficiency of Si-NSs. During cycling test, a current density of 0.1 C (0.42 A g^{-1}) is applied in the initial 5 cycles and the current density is maintained at a high level of 2 C (8.4 A g^{-1}) from the 6th to the 1000th cycle. Results show that even with such a high current density, a reversible capacity of 1126 mAh g^{-1} can be achieved after 300 cycles. Although the reversible capacity of Si-NSs is fading upon long-term cycling, the reversible capacity is still higher than 800 mAh g^{-1} after 900 cycles. Even after the cell is let stand for 10 days, the anode can have a capacity higher than 590 mAh g^{-1} after 1000 more cycles (see Fig. S5). For comparison, Table S1 lists the electrochemical performances of some Si-based anodes reported. The ultrathin nanosheets and the large surface area induced by the pores can facilitate the fast lithium insertion-extraction and the electron transport, which enables the anode to bear large current density. Additionally, the internal pores can accommodate the large lithiation-induced volume expansion, which helps protect the structural integrity of the electrodes and ensures the excellent cycling stability.⁴⁹

To further demonstrate the stability of Si-NSs, the half-cells after cycling tests are disassembled and the Si-NSs electrodes are investigated. Fig. S6 compares the morphology of the electrode material on the current collector between Si-NSs and the commercial nano-Si particle. Obviously, good attachment of Si-NSs anode with the copper current collector is maintained. In contrast, the Si particle electrode largely detaches from the copper current collector, which should be responsible for the capacity fade. SEM imaging on the cross-section of the Si-NSs before and after cycling are carried out, as shown in Fig. 3a and b respectively. It can be observed that the Si-NSs electrode maintains the original integrity and exhibits only 17% change in thickness after cycling,

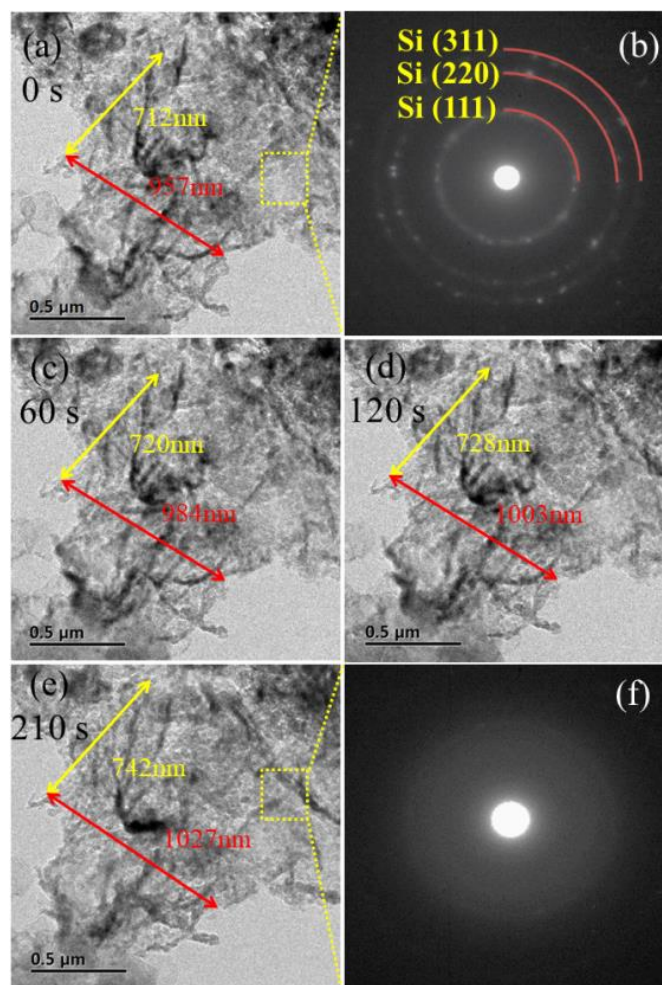


Fig. 4. In-situ TEM observation of the lithiation process of Si-NSs. (a, c, d, e) Time-resolved TEM images of Si-NSs upon lithiation. SAED images of Si-NSs (b) before and (f) after lithiation.

reconfirming the superior structural stability of the Si-NSs electrodes. The Si-NSs after cycling is disassembled and rinsed with dimethyl carbonate. Fig. 3c and d show the morphology of the electrode. It can be seen that the porous structure of the Si-NSs still exists after these charging-discharging cycles. Such good stability can be ascribed to the porous nature of the as-synthesized Si-NSs. For non-porous active material reported, porous structure can also be created by the lithiation-induced expansion and diffusion of the lithium ions,⁵⁰⁻⁵² but the integrity of the anode and the contact with current collector are damaged due to the drastic deformation.

In-situ TEM experiment is performed to show the structural evolution during lithiation process. The setup of the half-cell used for the in-situ TEM test is illustrated in Fig. 4a. Fig. 4a and c-e show the microstructural evolution of Si-NSs during the in-situ lithiation process which lasted for 210 s. Lithiation would happen once the Si-NSs contact the $\text{Li}_2\text{O}/\text{Li}$ electrode and a negative potential of -10 V is applied to the nanosheets. At the beginning of the experiment (Fig. 4b), the rings of the SAED

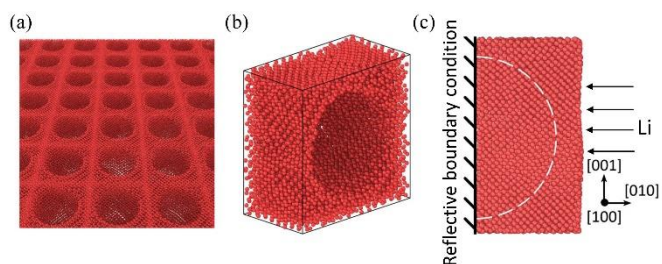


Fig. 5. Illustration of the simulation model with an initial porosity of 20%. (a) A global view of the simulated porous sheet. (b) The view of the unit cell from [221] direction. (c) The view of the unit cell from [100] direction. Periodic boundary conditions are used along [100] and [001] directions to represent an infinitely large sheet. A reflective boundary condition is applied to reduce the computational consumption. The white dashed line shows the profile of the pore. Lithiation occurs along the [010] direction.

pattern (inset in Fig. 4b) correspond to crystalline silicon can be observed, and after 210 s, the Si-NSs are fully lithiated and the structure transforms from crystalline into amorphous (Fig. 4f). The change of distances between two pairs of material points is tracked, as shown in Fig. 4a and c-e. The linear strain of our Si-NSs is estimated to be on the order of magnitude of a few tens of percent, which is smaller than the other Si electrodes as reported in the literature.^{50,53,54} The volume expansion is significantly reduced due to the unique 2D porous structure and the well-organized Si nanocrystals. Thus the lithiation-induced pulverization is prevented and stable electrochemical performances are achieved.

Molecular Dynamics (MD) simulation for the performance of the porous Si-NSs

In order to further explain the outstanding electrochemical performances of our porous Si-NSs electrodes from an atomistic perspective, we conduct molecular dynamics (MD) simulation, which has been proved capable in modeling the alloying process between Li and Si.³⁶⁻⁴³ In accordance with the SEM images of the porous Si-NSs (Fig. 1a), four crystalline porous Si-NSs electrode models with different initial porosities (including three porous models: 20%, 37% and 58%, and a solid counterpart) are constructed. Here, the pores are modelled as hollow hemispheres (see Fig. 5), and a specific porosity of the sheet is obtained by tuning the diameter of the hemisphere. Cyclic lithiation-delithiation processes are simulated. The mass capacity and the volumetric capacity of each electrode after 10 cycles are investigated; the porosity of each electrode after each cycle is also calculated based on the obtained atomistic configuration. Because the initial coulombic efficiency of the anode (see Fig. 2e) is less than 100%, here we consider a partial delithiation mode, in which the Li atoms are partially extracted from the anode during the delithiation. Fig. S6 elaborates the simulation of partial delithiation. More details regarding the MD simulations are available in Methods and Supplementary Material.

The normalized mass capacity, c_m , of each electrode is calculated based on the number of Li atoms extracted during

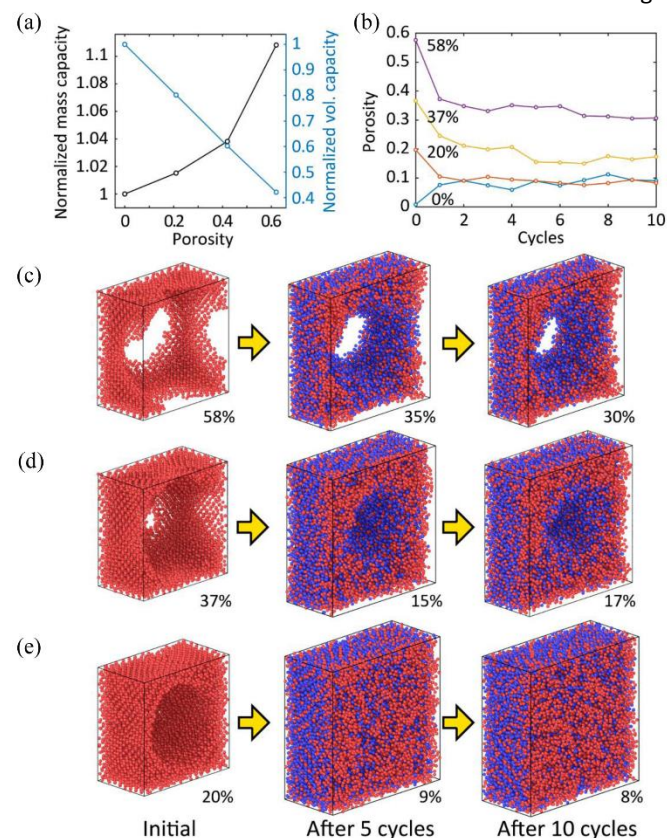


Fig. 6. (a) The mass (black line) and volumetric (blue line) capacities of anodes with different initial porosity after 10 lithiation-delithiation cycles. (b) The evolution of the porosity of the different porous Si-NSs anodes with the cycle number. (c), (d) and (e) The developments of the porous structure during lithiation-delithiation cycles of the anodes with initial porosity of (c) 58 % (d) 37 %, and (e) 20 %. Red and blue spheres represent Si and Li atoms, respectively. The percentage under each panel is the current porosity of the structure. The left, middle, and right panels show the porous structure in initial state, after 5 lithiation-delithiation cycles, and after 10 cycles, respectively.

delithiation process and then normalized by that of the solid (non-porous) one. The normalized volumetric capacity, c_v , can be obtained from the equation $c_v = c_m(1 - \phi)$, where ϕ stands for the initial porosity of the anode. Fig. 6a shows the calculation results of the normalized mass and volumetric capacities. It can be seen that as the initial porosity increases, the mass capacity also increases while the volumetric capacity decreases, indicating that improving both mass and volumetric capacities simultaneously is a challenge. There is a trade-off between the mass capacity and the volumetric capacity for an anode material. The selection of the optimal porosity depends on whether volume or mass is the dominant concern for the particular application.

To elucidate the underlying dependence of the capacity on the initial porosity, we examine the evolution of the porosity within the 10 cycles, as shown in Fig. 6b. The porosity of the porous electrode drops after 10 cycles, implying that the volume occupied by the lithiation-induced expansion cannot be fully recovered after delithiation. This is basically due to the plastic deformation of the ductile lithiated Si.⁵⁵⁻⁶⁰ In contrast, the porosity of the solid (non-porous) electrode grows with the cycling number, implying that solid (non-porous) electrode becomes porous after lithiation-delithiation cycles. Fig. 6c, d and e graphically show the evolutions of the atomistic porous structure for the three porous cases shown in Fig. 6b. The evolution of the porous structure in combination with the profile of mass capacity indicates that electrodes with higher initial porosity would exhibit higher mass capacity after 10 cycles. This is reasonable because porous structure can increase the surface area of the electrode and thus reduce the diffusion distance of Li in Si during lithiation and delithiation processes, which facilitates the Li atoms to move in and out of the surface of Si. As some of the Li atoms that participate in the initial lithiation process are unable to be extracted from the electrode in the subsequent processes due to various reasons (e.g. formation of SEI, etc.), only those Li atoms (the “active” Li atoms) capable of shuttling between electrode and electrolyte constitute the stable mass capacity of the electrode. In other words, porous structure enhances the amount of “active” Li atoms during the stable stage of the cycling and consequently promotes the mass capacity. The longer the porous structure survives, the longer the high mass capacity can be retained.

Conclusions

In this paper, porous Si nanosheets were prepared for evaluating electrochemical performance and illustrating evolution and survivability of porous structures during cycling. The unique structure of the porous Si-NSs facilitates effective transportations of electrons and lithium ions and largely enhances the electrochemical performances including the specific capacity, lifespan and rate capability. The economic fabrication processes of the porous Si-NSs are believed to help reduce the fabrication cost of LIBs. Molecular dynamics simulation is applied to study the relationship between capacity and the porosity during lithiation-delithiation cycling, giving an explanation to the excellent electrochemical performances of the Si-NSs. We believe that our work would not only facilitate the design of 2D material as energy material, but also promote the advent of the next generation LIBs.

Conflicts of interest

There are no conflicts to declare.

Acknowledgements

We acknowledge financial support from the Research Grants Council of the Hong Kong Special Administration Region (PolyU

5293/13E, PolyU 152064/15E), the Hong Kong Polytechnic University (Grants No. G-YBLF, 1-ZVJD, 1-ZVGH and G-YW0M) and the National Natural Science Foundation of China (51802354, 51871247). QL gratefully acknowledges the financial supporting of National Science Foundation of China (Grant No. 51702207).

Notes and references

- J. M. Tarascon, M. Armand, *Nature*, 2001, **414**, 359-367.
- M. Armand, J. M. Tarascon, *Nature*, 2008, **451**, 652.
- J. W. Choi, D. Aurbach, *Nature Reviews Materials*, 2016, **1**, 16013.
- J. Liu, P. Kopold, P. A. Aken, J. Maier, Y. Yu, *Angew. Chem. Int. Ed.*, 2015, **54**, 9632-9636.
- S. Choi, T. Kwon, A. Coskun, J. W. Choi, *Science*, 2017, **21**, 279-283.
- W. M. Zhang, J. S. Hu, Y. G. Guo, S. F. Zheng, L. S. Zhong, W. G. Song, L. J. Wan, *Adv. Mater.*, 2008, **20**, 1160-1165.
- W. Dong, J. Xu, C. Wang, Y. Lu, X. Liu, X. Wang, X. Yuan, Z. Wang, T. Liu, M. Sui, I. W. Chen, F. Huang, *Adv. Mater.*, 2017, **29**, 1700136.
- S. Zhu, J. Li, X. Deng, C. He, E. Liu, F. He, C. Shi, N. Zhao, *Adv. Funct. Mater.*, 2017, **27**, 160517.
- T. Hoshida, Y. Zheng, J. Hou, Z. Wang, Q. Li, Z. Zhao, R. Ma, T. Sasaki, F. Geng, *Nano Lett.*, 2017, **17**, 3543-3549.
- J. Wang, H. Tang, L. Zhang, H. Ren, R. Yu, Q. Jin, J. Qi, D. Mao, M. Yang, Y. Wang, P. Liu, Y. Zhang, Y. Wen, L. Gu, G. Ma, Z. Su, Z. Tang, H. Zhao, D. Wang, *Nat. Energy*, 2016, **1**, 16050.
- C. Kim, K. S. Yang, M. Kojima, K. Yoshida, Y. J. Kim, Y. A. Kim, M. Endo, *Adv. Funct. Mater.*, 2006, **16**, 2393-2397.
- X. Zhang, G. Zhu, M. Wang, J. Li, T. Lu, L. Pan, *Carbon*, 2017, **116**, 686-694.
- M. N. Obrovac, L. Christensen, *Electrochem. Solid-State Lett.*, 2004, **7**, A93-A96.
- B. Key, R. Bhattacharyya, M. Morcrette, V. Seznec, J. M. Tarascon, C. P. Grey, *J. Am. Chem. Soc.*, 2009, **131**, 9239-9249.
- Y. Son, S. Sim, H. Ma, M. Choi, Y. Son, N. Park, J. Cho, M. Park, *Adv. Mater.*, 2018, **30**, 1705430.
- H. Song, H. X. Wang, Z. Lin, X. Jiang, L. Yu, J. Xu, Z. Yu, X. Zhang, Y. Liu, P. He, L. Pan, Y. Shi, H. Zhou, K. Chen, *Adv. Funct. Mater.*, 2016, **26**, 524-531.
- S. H. Ng, J. Z. Wang, D. Wexler, K. Konstantinov, Z. P. Guo, H. K. Liu, *Angew. Chem. Int. Ed.*, 2006, **45**, 6896-6899.
- S. Chen, L. Shen, P. A. Aken, J. Maier, Y. Yu, *Adv. Mater.*, 2017, **29**, 1605650.
- N. Liu, H. Wu, M. T. McDowell, Y. Yao, C. M. Wang, Y. Cui, *Nano Lett.*, 2012, **12**, 3315-3321.
- W. Wang, Z. Favors, R. Ionescu, R. Ye, H. H. Bay, M. Ozkan, C. S. Ozkan, *Scientific Reports*, 2015, **5**, 8781.
- L. F. Cui, R. Ruffo, C. K. Chan, H. L. Peng, Y. Cui, *Nano Lett.*, 2009, **9**, 491-495.
- C. E. Ren, M. Q. Zhao, T. Makaryan, J. Halim, M. Boota, S. Kota, B. Anasori, M. W. Barsoum, Y. Gogotsi, *ChemElectroChem*, 2016, **3**, 689-693.
- L. Peng, Y. Zhu, D. Chen, R. S. Ruoff, G. Yu, *Adv Energy Mater.*, 2016, **6**, 11.
- C. Chen, X. Xie, B. Anasori, A. Sarycheva, T. Makaryan, M. Zhao, P. Urbankowski, L. Miao, J. Jiang, Y. Gogotsi, *Angew. Chem.*, 2018, **130**, 1864-1868.
- J. Ryu, D. Hong, S. Choi, S. Park, Synthesis of Ultrathin Si Nanosheets from Natural Clays for Lithium-Ion Battery Anodes, *ACS Nano*, 2016, **10**, 2843-2851.
- W. S. Kim, Y. Hwa, J. H. Shin, M. Yang, H. J. Sohn, S. H. Hong, *Nanoscale*, 2014, **6**, 4297-4302.

- 27 H. P. Jia, P. F. Gao, J. Yang, J. L. Wang, Y. N. Nuli, Z. Yang, *Adv. Energy Mater.*, 2011, **1**, 1036-1039.
- 28 M. Y. Ge, J. P. Rong, X. Fang, C. W. Zhou, *Nano Lett.*, 2012, **12**, 2318-2323.
- 29 L. D. Lin, X. N. Xu, C. X. Chu, M. K. Majeed, J. Yang, *Angew. Chem. Int. Ed.*, 2016, **55**, 14063-14066.
- 30 W. S. Hummers Jr, R. E. Offeman, *J. Am. Chem. Soc.*, 1958, **80**, 1339-1339.
- 31 J. J. Tang, G. H. Chen, J. Yang, X. Y. Zhou, L. N. Zhou, B. Huang, *Nano Energy*, 2014, **8**, 62-70.
- 32 S. Plimpton, *J. Comput. Phys.*, 1995, **117**, 1-19.
- 33 H. M. Aktulga, J. C. Fogarty, S. A. Pandit, A. Y. Grama, *Parallel Comput.*, 2012, **38**, 245-259.
- 34 A. K. Rappe, W. A. Goddard III, *J. Phy. Chem.*, 1991, **95**, 3358-3363.
- 35 A. Nakano, *Comput. Phys. Commun.*, 1997, **104**, 59-69.
- 36 A. Ostadhosseini, E. D. Cubuk, G. A. Tritsarlis, E. Kaxiras, S. Zhang, A. C. van Duin, *Phys. Chem. Chem. Phys.*, 2015, **17**, 3832-3840.
- 37 F. F. Fan, S. Huang, H. Yang, M. Raju, D. Datta, V. B. Shenoy, A. C. T. van Duin, S. L. Zhang, T. Zhu, *Modell. Simul. Mater. Sci. Eng.*, 2013, **21**, 074002.
- 38 H. Jung, M. Lee, B. C. Yeo, K. R. Lee, S. S. Han, *J. Phys. Chem. C*, 2015, **119**, 3447-3455.
- 39 K. J. Kim, Y. Qi, *J. Phys. Chem. C*, 2015, **119**, 24265-24275.
- 40 S. P. Kim, D. Datta, V. B. Shenoy, *J. Phys. Chem. C*, 2014, **118**, 17247-17253.
- 41 S. Y. Kim, A. Ostadhosseini, A. C. T. van Duin, X. C. Xiao, H. J. Gao, Y. Qi, *Phys. Chem. Chem. Phys.*, 2016, **18**, 3706-3715.
- 42 H. S. Lee, B. J. Lee, *Met. Mater. Int.*, 2014, **20**, 1003-1009.
- 43 X. J. Wang, F. F. Fan, J. W. Wang, H. R. Wang, S. Y. Tao, A. Yang, Y. Liu, H. B. Chew, S. X. Mao, T. Zhu, S. M. Xia, *Nat. Comm.*, 2015, **6**, 8417.
- 44 H. J. C. Berendsen, J. P. M. Postma, W. F. Vangunsteren, A. Dinola, J. R. Haak, *J. Chem. Phys.*, 1984, **81**, 3684-3690.
- 45 A. Stukowski, *Modell. Simul. Mater. Sci. Eng.*, 2010, **18**, 015012.
- 46 D. C. Marcano, D. V. Kosynkin, J. M. Berlin, A. Sinitskii, Z. Z. Sun, A. Slesarev, L. B. Alemany, W. Lu, J. M. Tour, *ACS Nano*, 2010, **4**, 4806-4814.
- 47 X. Y. Yue, Z. Yan, Y. Song, X. J. Wu, Y. N. Zhou, *Nanoscale*, 2018, **10**, 19195-19202.
- 48 Y. Chen, L. F. Liu, J. Xiong, T. Z. Yang, Y. Qin, C. L. Yan, *Adv. Funct. Mater.*, 2015, **25**, 6701-6709.
- 49 X. Y. Yue, A. Abulikemu, X. L. Li, Q. Q. Qiu, F. Wang, X. J. Wu, Y. N. Zhou, *J. Power Sources*, 2019, **410-411**, 132-136.
- 50 M. Gu, Y. Li, X. L. Li, S. Y. Hu, X. W. Zhang, W. Xu, S. Thevuthasan, D. R. Baer, J. G. Zhang, J. Liu, C. M. Wang, *ACS Nano*, 2012, **6**, 8439-8447.
- 51 X. H. Liu, S. Huang, S. T. Picraux, J. Li, T. Zhu, J. Y. Huang, *Nano Lett.*, 2011, **11**, 3991-3997.
- 52 J. W. Choi, J. McDonough, S. Jeong, J. S. Yoo, C. K. Chan, Y. Cui, *Nano Lett.*, 2010, **10**, 1409-1413.
- 53 C. F. Shen, M. Y. Ge, L. L. Luo, X. Fang, Y. H. Liu, A. Y. Zhang, J. P. Rong, C. M. Wang, C. W. Zhou, *Sci. Rep.*, 2016, **6**, 31334.
- 54 X. H. Liu, L. Zhong, S. Huang, S. X. Mao, T. Zhu, J. Y. Huang, *ACS Nano*, 2012, **6**, 1522-1531.
- 55 A. F. Bower, P. R. Guduru, *Modell. Simul. Mater. Sci. Eng.*, 2012, **20**, 045004.
- 56 A. F. Bower, P. R. Guduru, E. Chason, *Int. J. Solids Struct.*, 2015, **70**, 328-342.
- 57 A. F. Bower, P. R. Guduru, V. A. Sethuraman, *J. Mech. Phys. Solids*, 2011, **59**, 804-828.
- 58 Y. Y. Lu, Y. Ni, *Mech. Mater.*, 2015, **91**, 372-381.
- 59 K. J. Zhao, M. Pharr, S. Q. Cai, J. J. Vlassak, Z. G. Suo, *J. Am. Ceram. Soc.*, 2011, **94**, S226-S235.
- 60 K. J. Zhao, M. Pharr, Q. Wan, W. L. Wang, E. Kaxiras, J. J. Vlassak, Z. G. Suo, *J. Electrochem. Soc.*, 2012, **159**, A238-A243.